Jensen–Shannon Distance-Based Filter and Unsupervised Evaluation Metrics for Polarimetric Weather Radar Processing

Chen, Cheng ; Unal, Christine M. H.; Oude Nijhuis, Albert C.P.

DOI
10.1109/TGRS.2022.3200731

Publication date
2022

Document Version
Final published version

Published in
IEEE Transactions on Geoscience and Remote Sensing

Jensen–Shannon Distance-Based Filter and Unsupervised Evaluation Metrics for Polarimetric Weather Radar Processing

Cheng Chen, Christine M. H. Unal, and Albert C. P. Oude Nijhuis

***Abstract*— An effective filtering technique is required for rainfall rate measurement by weather radar. A Jensen–Shannon distance (JSD)-based thresholding filter is proposed to mitigate nonmeteorological signals, either in clear air or rain situations. This algorithm classifies range-Doppler bins into two classes, hydrometeors and nonhydrometeors, based on spectral polarimetric variable features. The result is a mask to be applied on the spectrograms. The variable selected here is the spectral co-polar correlation coefficient, available in dual-polarization and full polarimetric radars. The algorithm first does global thresholding by finding an optimized threshold value based on the averaged clear-air spectral polarimetric variable distribution. Next, classical filtering steps are carried out like a ground clutter notch filter around 0 ms^{-1}, a mathematical morphology to fill gaps in the hydrometeor areas, and a removal of narrow Doppler power spectra. The second part of this article is the assessment of filtering techniques without ground truth. An assessment without ground truth is useful to select optimal algorithm configurations from a large solution space. Criteria of good filtering are defined both in the spectral and time domain. Based on those criteria, subjective and objective unsupervised evaluation metrics are derived, with a focus on the objective ones. Data, including clear air and rain collected from a full polarimetric Doppler X-band radar in the urban area, are used. With the proposed unsupervised evaluation metrics, the JSD-based thresholding filter is compared to two spectral polarimetric filters. Overall, the JSD-based filter performs very well considering both the subjective and the objective evaluation metrics.**

***Index Terms*— Adaptive thresholding, dual-polarization weather radar, spectral polarimetric filtering of nonhydrometeors, unsupervised evaluation metrics.**

I. Introduction

EUROPE's cities are facing increased risks due to severe precipitation driven by climate change combined with rapid urbanization and population growth [1]. Monitoring rainfall in the city at street level is an efficient way to improve urban weather resilience. The temporal and spatial resolutions of rainfall data required for urban applications exceed those needed for rural catchments. Nonetheless, current monitoring systems are not adapted and often inaccurate at city scale, making such rainfall information ineffective for urban applications [2]. With X-band radars, the study of rainfall mechanisms at high resolution can be performed on a regional scale. Yet, the accurate estimation of rainfall data in real time in dense urban areas using this sensor is challenging due to clutter [2].

Clutter can be decomposed into two types: stationary and nonstationary. The stationary clutter is termed ground clutter and is located at the 0-ms^{-1} Doppler velocity with variable spectral widths. A classical technique uses a notch filter centered at 0 ms^{-1}. To strengthen this technique, the Clutter Environment Analysis using Adaptive Processing (CLEAN-AP), which is based on the autocorrelation spectral density, was proposed [3] to meet the Next Generation Weather Radar (NEXRAD) clutter mitigation requirements. Good performance is obtained in terms of ground clutter mitigation and reduction in the variance of weather radar variables. However, the nonstationary clutter, which is located at variable Doppler velocity bins, stays. Therefore, methodologies, exploring the use of spectral polarimetry only [4], [5] or combined with fuzzy logic [6] or image processing techniques [7], [8], were proposed to reduce both stationary and nonstationary clutter and mitigate noise. The combination with fuzzy logic or image processing was added for low elevation angle atmospheric/weather radar measurements.

Using spectral polarimetry filtering, this article first focuses on urban clutter (stationary and nonstationary) and noise reduction, using the data of the Rijnmond radar in Rotterdam. The techniques proposed in this article are meant to be implemented in other X-band radars as well: MESEWI on the campus of the Delft University of Technology (urban area) and IDRA in Cabauw (polder area). These three X-band radars are integrated within the National Ruisdael Observatory, a research infrastructure to study atmospheric processes at different spatial and temporal scales linking data and models for climate change, weather, and air quality predictions. The major steps of the clutter and noise mitigation, alternatively labeled as "nonmeteorological echoes mitigation," are made in the range-Doppler domain. The strength of spectral polarimetric processing is that it can remove nonmeteorological echoes in the Doppler domain, while they overlap with precipitation in the time domain. In addition, weak precipitation can be retained because of a decrease in the noise level in the

Manuscript received 7 April 2022; revised 5 July 2022; accepted 5 August 2022. Date of publication 23 August 2022; date of current version 12 September 2022. This work was supported in part by the EC through the ATTRACT Project [Enhanced Urban Rain Surveillance Systems for Smart City Solutions (EU-RainS4)] under Grant 777222. *(Corresponding author: Cheng Chen.)*

The authors are with the Department of Geoscience and Remote Sensing, Faculty of Civil Engineering and Geoscience, Delft University of Technology, 2628 CN Delft, The Netherlands (e-mail: cardistcc@outlook.com; c.m.h.unal@tudelft.nl; albertoudenijhuis@sky-echo.eu).

Digital Object Identifier 10.1109/TGRS.2022.3200731

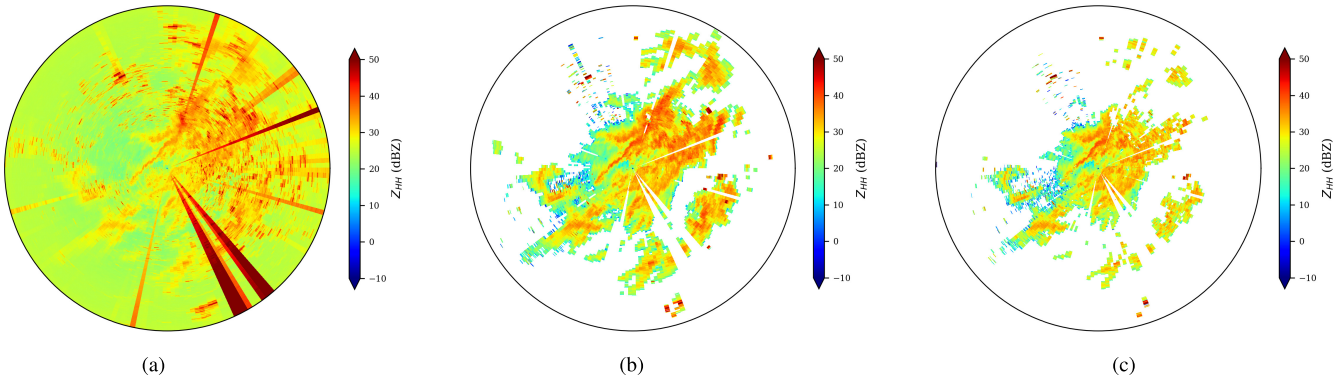

Fig. 1. Example of PPI plots of the radar reflectivity from the Rijnmond radar: (a) raw data and (b) and (c) use the OBSpol filtering method [8] with different fixed thresholds on the spectral co-polar correlation coefficient (0.90 $s\rho_{\text{co}}$-threshold and 0.95 $s\rho_{\text{co}}$-threshold, respectively).

spectral domain. Some of the mentioned spectral polarimetric filtering methods are based on radar variable thresholding such as the spectral linear depolarization ratio [5], [7], [8] and the spectral co-polar correlation coefficient [4], [8].

Global thresholding plays an essential role in the reduction of nonmeteorological echoes. Such methods are based on thresholding with a fixed value, which provides fast processing for real-time applications. However, they may not be robust. As concluded from [9, p. 517], when polarimetric variables are used for classification, their magnitudes differ for various situations.

Let us now consider the following three plan position indicators (PPIs) in Fig. 1. The first PPI represents raw data of precipitation, which are not filtered and thus still contain clutter and noise. With the choice of a threshold of 0.95 [Fig. 1(c)] for the spectral co-polar correlation coefficient, a significant amount of precipitation disappears while being preserved for a threshold choice of 0.90 [Fig. 1(b)]. What is the meaning of these values, 0.90 and 0.95? This threshold choice depends on so many factors, such as the type of radar, the radar environment, the processing, and the signal-to-noise ratio (SNR). This article proposes a new spectral polarimetric filtering technique with a focus on the methodology and not on the actual threshold values.

Coming back to Fig. 1, we can probably say that a threshold of 0.90 [Fig. 1(b)] is better than a threshold of 0.95 [Fig. 1(c)] based on a subjective evaluation. However, assessment criteria should be developed to quantitatively compare filtered PPIs or spectrograms without ground truth. This is the second objective of this article: evaluation by metrics without ground truth.

There are no common standards for filtering assessment in the mentioned references where spectral polarimetric processing is used, which makes it challenging to define objective evaluation metrics. In addition, the used assessment methods may not be suitable for testing large amounts of data (spectrograms and PPIs for at least several days). It is challenging to always generate ground-truth data. This is the key issue: nonhydrometeor mitigation evaluation without ground truth.

Some assessment studies are done in the field of image segmentation, but those methods still need to be validated for range-Doppler spectrograms. Another solution considers time-series data corresponding to weather signal free of clutter contamination, which can be added with that of clutter signal obtained in clear-air conditions [10], [11]. This solution allows the analysis of bias of radar variable estimates, which are involved in rainfall rate estimators. For the Rijnmond radar, it is possible to obtain IQ data of clear air without hydrometeor presence. However, rain data with the certainty to measure no clutter cannot be acquired at low elevation angles in an urban environment with a limited maximum range. In addition, such a methodology or external validation using a network of rain gauges and/or disdrometers is only achievable for a very small set of radar and algorithm configurations and sufficient collection of data. This is due to the nature of the raw weather radar IQ data. Their amount is very large and hard to store and process for many different parameters for a long period. Nonetheless, a long period is required to obtain sufficient statistics for a valid comparison. If we have weather radar processing algorithms that have a very large solution space of configurations (combination of parameters and different algorithms), it becomes very challenging to use assessment adding hydrometeor and clutter data or external validation for so many parameters. We need thus to significantly reduce the solution space of radar processing algorithms first.

For this objective, image segmentation assessment criteria will be explored. They allow a first evaluation of filtering techniques in the range-Doppler domain. With this approach, a reduced set of techniques and possible configurations can be obtained and finally assessed using the analysis of radar variable bias and/or quantitative precipitation estimation (QPE) validation techniques.

This article is structured as follows: Section II introduces the data used in this article, the specifications of the radar, and an overview of the default Rijnmond radar filtering algorithm, presently implemented in the radar real-time processing. The construction of the new filtering algorithm is presented in Section III. In Section IV, the unsupervised evaluation metrics to assess filtering techniques are explained. Section V assesses the performance of three different filters and their results are discussed in Section VI. Finally, Section VII draws the conclusions.

TABLE I
RIJNMOND RADAR SPECIFICATIONS

Max.transmitted power	43 dBm
Attenuation (power reduction)	Automatic
Transmitted polarisation	H or V
Received polarisation	H+V
Central frequency	9.325 GHz
Sampling rate	10 MHz
Number of samples	3050
Sweep time	305 μs
Number of range bins	1525
Bandwidth	7.5 MHz
Range resolution	0.02 km
Maximum range	30.5 km
Number of Doppler bins	512
Doppler resolution	0.0515 ms^{-1}
Maximum Doppler velocity (ATSR)	13.18 ms^{-1}
Dwell time	0.31 s

II. RADAR SPECIFICATIONS AND DATASET

A. Specifications of Rijnmond Radar

Table I lists the specifications of the Rijnmond radar dataset that is used in this article. This frequency-modulated continuous-wave (FMCW) radar operates at X-band with a central frequency of 9.325 GHz. It is a full polarimetric radar with an alternate transmission simultaneous reception (ATSR) polarimetric configuration. Its default rotation speed is 6.0° s^{-1}, so a whole PPI measurement needs 1 min.

The high range resolution of 20 m is appropriate for urban applications. The maximum Doppler velocity equals 26.36 ms^{-1}. However, because horizontal and vertical polarization are alternated in transmission, the time between two consecutive samples with the same polarization becomes larger by a factor of 2, which decreases the maximum Doppler velocity by a factor of 2, thus 13.18 ms^{-1}. With 512 samples for the Doppler processing, a high Doppler velocity resolution of 5.15 cm/s is obtained, which offers possibilities in mitigating noise and urban clutter using spectral processing.

B. Dataset

The dataset is classified in two scenarios, namely, clear air and rain. The clear air refers to all the signals from nonhydrometeors and noise. The clear-air dataset contains two PPIs. The first PPI (reference) is used to develop the algorithm and the second PPI is considered for performance testing by different filtering techniques. Every rain case consists of one PPI. These different rain cases are selected to include light, moderate, and heavy precipitation with little, moderate, or heavy clutter. All of them are going to be used for obtaining the results of the objective evaluation metrics in Section V.

Table II lists the start and end measurement time and characteristics of each PPI. The clear-air case consists of two PPIs. The term "variable rain" indicates that the PPI contains light, moderate, and heavy rain. These input data have the same radar specifications (Table I) except for the transmit power/ receiver gain reduction and elevation angle. In the case of automatic signal attenuation, the attenuation is increased on-the-fly to reduce signal saturation issues. A radar ray that is suffering from saturation can be recognized by a radar ray line with very high reflectivity [see, e.g., Fig. 1(a)].

C. Default Rijnmond Filtering

Presently, the filtering for noise and clutter mitigation is carried out in the range-Doppler domain. It consists of a narrow notch filter centered around 0 ms^{-1} (ground clutter suppression) and spectral polarimetric filtering with fixed thresholds. Furthermore, a spectral noise clipping technique is implemented. It keeps the Doppler bins related to a spectral power at least 3 dB above the spectral noise level (noise suppression). Finally, Doppler spectra containing less than 2% of valid Doppler bins are discarded. Therefore, it is expected to retain the Doppler bins related to precipitation. Consequently, the standard radar moments and polarimetric variables can be calculated. This filtering technique is presently applied for three X-band radars in The Netherlands: the Rijnmond radar at Rotterdam, MESEWI at the TU Delft campus, and IDRA at Cabauw.

III. JENSEN–SHANNON DISTANCE-BASED THRESHOLDING FILTER

A. Spectral Polarimetric Variables

The complex spectrogram S_{XY} is used in the calculation of spectral polarimetric variables, with X and Y being the polarization in reception and transmission, respectively [12]. The corresponding spectral reflectivity is defined as

$$sZ_{XY}(r,v) = C_{XY} \cdot |S_{XY}(r,v)|^2 \cdot r^2 = C_{XY} \cdot P_{XY}(r,v) \cdot r^2 \tag{1}$$

where C_{XY} represents a constant depending on the polarizations, r is the range, v is the Doppler velocity, and $P_{XY}(r,v)$ is the received power for each range-Doppler bin.

The following four spectral polarimetric variables, sZ_{DR}, $sL_{\text{DR}}^{\text{HH}}$, $sL_{\text{DR}}^{\text{VV}}$, $s\rho_{\text{co}}$ are defined based on S_{XY} and sZ_{XY}:

$$sZ_{\text{DR}}(r,v) = 10\log_{10}\left(\frac{sZ_{\text{HH}}(r,v)}{sZ_{\text{VV}}(r,v)}\right) \tag{2}$$

$$sL_{\text{DR}}^{\text{HH}}(r,v) = 10\log_{10}\left(\frac{sZ_{VH}(r,v)}{sZ_{\text{HH}}(r,v)}\right) \tag{3}$$

$$sL_{\text{DR}}^{\text{VV}}(r,v) = 10\log_{10}\left(\frac{sZ_{HV}(r,v)}{sZ_{\text{VV}}(r,v)}\right) \tag{4}$$

$$s\rho_{\text{co}}(r,v) = \frac{\left|\left\langle S_{\text{HH}}(r,v)S_{\text{VV}}^{*}(r,v)\right\rangle\right|}{\sqrt{\left\langle|S_{\text{HH}}(r,v)|^2\right\rangle\left\langle|S_{\text{VV}}(r,v)|^2\right\rangle}} \tag{5}$$

where $\langle\rangle$ is the 2-D averaging on consecutive range-Doppler pixels.

In this work, the 2-D averaging for the cross correlation calculation is done by using a square averaging kernel $n_k \times n_k$ with a kernel of size $n_k = 7$. The choice of $n_k = 7$ leads to a better estimate of the variables for filtering (more averaged/smoothed) at the cost of the Doppler velocity resolution. This will only impact the classification mask in the filtering technique. Note that the estimation of the time-domain variables, such as reflectivity factor and co-polar correlation coefficient, is not impacted, as for such calculations, no (additional) averaging is performed in the range-Doppler domain.

TABLE II
INPUT DATA

Scenario	Clear Air	Rain					
Case ID	0	1	2	3	4	5	6
Start time	2020-02-05 15:45:55	2020-02-04 13:09:20	2020-06-17 20:23:39	2020-09-23 18:33:14	2020-09-25 19:14:07	2020-09-26 23:54:20	2020-10-06 11:21:19
End time	2020-02-05 15:47:56	2020-02-04 13:10:21	2020-06-17 20:24:40	2020-09-23 18:34:15	2020-09-25 19:15:07	2020-09-26 23:55:20	2020-10-06 11:22:18
Characteristics	much clutter saturation	light rain much clutter	variable rain little clutter	variable rain large cell	variable rain much clutter	light rain sparse	heavy rain small cells

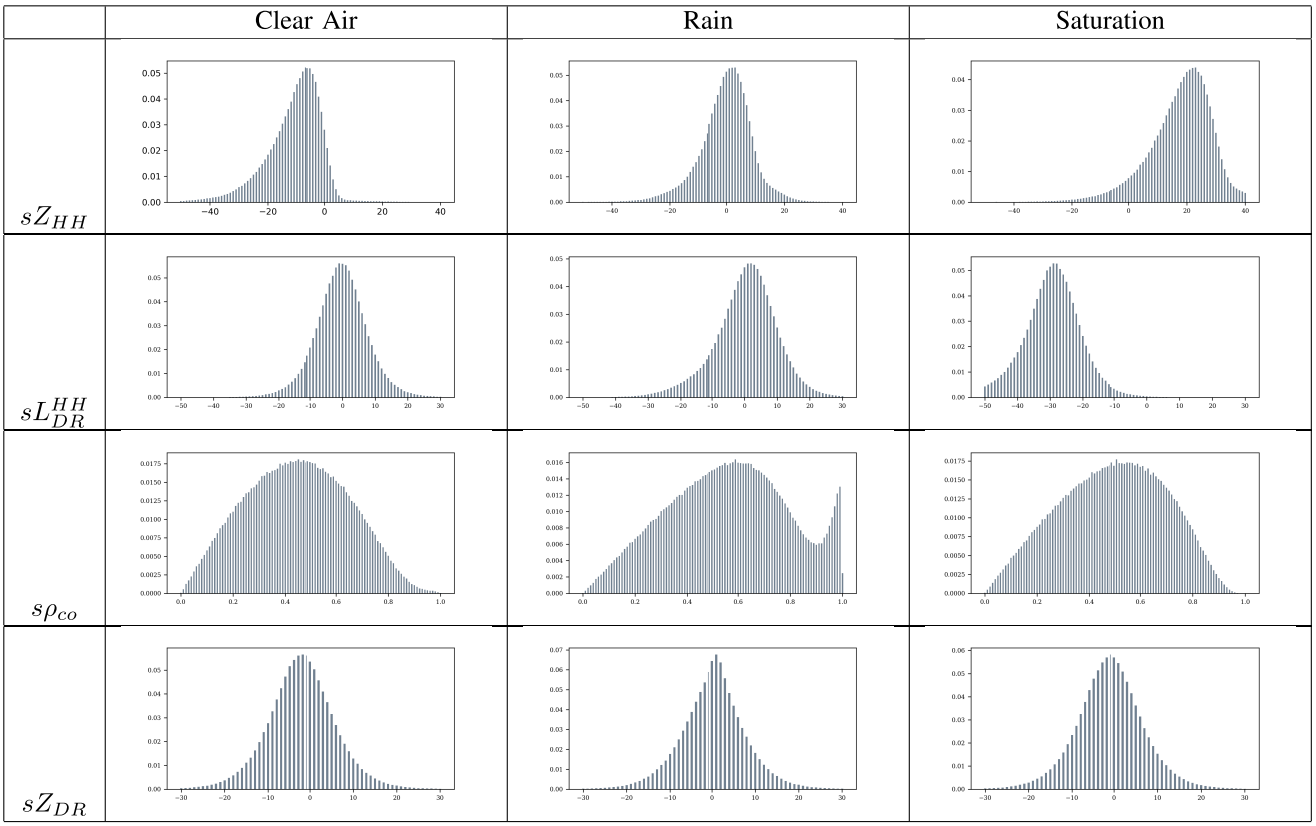

Fig. 2. Histograms of four spectral polarimetric variables from three different situations. The full raw spectrogram is considered. In the case of rain, there are thus range-Doppler bins with hydrometeors and nonhydrometeors.

B. Empirical Probability Functions of the Spectral Polarimetric Variables

When filtering techniques based on thresholding are designed, normalized histograms or equivalently empirical probability functions are investigated for different situations such as clear air, rain, and saturation.

Examples of saturation at some azimuthal directions (southeast) are shown in Fig. 1(a): a large signal, which is most likely caused by radio frequency interference (RFI), is measured by the FMCW radar. Because of the Fourier transform processing to get the backscattered power versus range, which is inherent to the FMCW radar, there is spectral leakage in all the range bins. Large power values are converted to reflectivity values using the weather equation [see (1)]. Because of the multiplication by r^2, the reflectivity values related to RFI increase with range.

Fig. 2 shows the examples of normalized histograms of the four spectral polarimetric variables for three different cases (clear air, rain, and saturation). The values of sZ_{HH}, sZ_{DR}, and sL_{DR} vary between -50 and 50 dB with a bin width of 1 dB. The values of $s\rho_{\mathrm{co}}$ vary between 0 and 1 with a bin width of 0.01. Each histogram relates to one raw spectrogram, which represents one PPI ray. In the case of rain presence, the spectral co-polar correlation coefficient probability function becomes bimodal, which is an interesting feature. All the range-Doppler bins are included in the histogram. For the rain case, there are thus spectra of rain, clutter, and noise but no saturation. Therefore, $s\rho_{\mathrm{co}}$ histogram contains a significant amount of low values. In the case of saturation, the histograms are shifted for the spectral reflectivity, sZ_{HH}, and for the linear depolarization ratios, toward larger and smaller values, respectively. This is not the case for $s\rho_{\mathrm{co}}$ and sZ_{DR} distributions, which allows to group clear air and saturation together as nonhydrometeor echoes. Next, a mathematical formulation, which uses probability functions, is used to design a new spectral polarimetric filter and assessment criteria to compare filters.

C. Shannon's Entropy

Information entropy or Shannon's entropy [13] is defined as the average logarithm of the inverse of probability. There are many interpretations of information entropy depending on its application. Here, it is used as measuring the number of states of a system. A large number of states, n, lead to high entropy, H. In the spectral polarimetric image context, the random variable X denotes one of the spectral polarimetric variables with $P_r(X = x_i)$ being its probability when having the value x_i, which is the ith possible value of X. This is mathematically formulated as

$$H(X) = \sum_{i=1}^{n} P(x_i) \log_2 \frac{1}{P(x_i)} \tag{6}$$

$$P(x_i) = Pr(X = x_i) \tag{7}$$

$$X \in \left\{ sZ_{\mathrm{DR}}, sL_{\mathrm{DR}}^{\mathrm{HH}}, sL_{\mathrm{DR}}^{\mathrm{VV}}, s\rho_{\mathrm{co}} \right\} \tag{8}$$

where the same discretization as for the histograms is used.

The fundamental properties of Shannon's entropy that will be used here are [14] given as follows.

1) $H(X)$ is a convex function and $H(X) \geq 0$.
2) $H(X)$ reaches its maximum value, $H(X)_{\max} = \log_2(n)$, when $P(x_1) = P(x_2) = \cdots = P(x_n) = 1/n$ (the number of values for the spectral polarimetric variable is large and the distribution of values is uniform).
3) $H(X)$ reaches its minimum, $H(X)_{\min} = 0$, when there is only one value possible for the spectral polarimetric variable.
4) For two statistical independent random variables X and Y, we have $H(X, Y) = H(X) + H(Y)$.

According to Properties 2 and 3, Shannon's entropy can be considered as a function of the distribution of a spectral polarimetric variable. This distribution or probability density function is estimated using the normalized histogram of spectral polarimetric variables. The properties of Shannon's entropy function are used to build assessment criteria for filtering in Section IV.

D. Jensen–Shannon Distance

Jensen–Shannon distance (JSD) is an entropy-based parameter, which is used to compare the similarity or discrepancy between distributions. Relatively low JSD values indicate similarity and thus less discrepancy between different distributions and vice versa. JSD is defined as the square root of Jensen–Shannon divergence [15]

$$\mathrm{JSD}(P \| Q) = \sqrt{\frac{1}{2} D_{\mathrm{KL}}(P \| M) + \frac{1}{2} D_{\mathrm{KL}}(Q \| M)} \tag{9}$$

$$D_{\mathrm{KL}}(P \| M) = \sum_{x \in \mathcal{X}} P(x) \log_2 \left(\frac{P(x)}{M(x)} \right) \tag{10}$$

$$D_{\mathrm{KL}}(Q \| M) = \sum_{x \in \mathcal{X}} Q(x) \log_2 \left(\frac{Q(x)}{M(x)} \right) \tag{11}$$

$$M = \frac{1}{2}(P + Q) \tag{12}$$

where P and Q are two different probability functions, M is the pointwise mean of P and Q, and D_{KL} is defined as the Kullback–Leibler divergence.

The advantage of using the Jensen–Shannon divergence in comparison to other metrics for similarity between distributions is that it is finite and symmetric [16].

E. Selection of the Spectral Polarimetric Variable

A sensitivity test is conducted to find the most sensitive polarimetric spectrogram to the presence of hydrometeors. For this purpose, the JSD is used to assess the difference between two distributions, clear air and rain. The JSD is estimated for four spectral polarimetric variable distributions (sZ_{DR}, $sL_{\mathrm{DR}}^{\mathrm{HH}}$, $sL_{\mathrm{DR}}^{\mathrm{VV}}$, and $s\rho_{\mathrm{co}}$), where the distribution with rain included is compared to a clear-air reference distribution. The spectral polarimetric distribution of clear air ($\overline{P_{\mathrm{cla}}(X)}$) is obtained from the averaged distribution of a full PPI

$$\overline{P_{\mathrm{cla}}(X)} = \frac{1}{n_r} \sum_{\alpha=0}^{2\pi} P_{\mathrm{cla}}(X, \alpha) \tag{13}$$

$$X \in \{ sZ_{\mathrm{DR}}, sL_{\mathrm{DR}}^{\mathrm{HH}}, sL_{\mathrm{DR}}^{\mathrm{VV}}, s\rho_{\mathrm{co}} \} \tag{14}$$

$$\alpha \in [0, 2\pi] \tag{15}$$

where $P_{\mathrm{cla}}(X, \alpha)$ is the distribution of one spectral polarimetric variable X at azimuth angle α and n_r is the total number of radar rays per PPI.

Fig. 3(a) shows the results of JSD between polarimetric spectrogram histograms with rain included and the averaged clear-air reference for a complete PPI. This figure demonstrates that $s\rho_{\mathrm{co}}$ has the highest sensitivity for the presence of rain. The fact that $s\rho_{\mathrm{co}}$ has the highest sensitivity from these variables is also consistent with characteristic change of distribution shape when rain appears, going from a monomodal to bimodal distribution in Fig. 2. For the other three variables, no distinct sensitivity is found. With respect to the raw PPI of rain [Fig. 3(b)], the JSD of $s\rho_{\mathrm{co}}$ has a positive correlation with the rain areas. For example, when the radar ray is around 100°, both the JSD and the nonfiltered reflectivity decrease dramatically indicating the absence of rain.

F. Filter Description

A new filtering technique is proposed in this research, which uses a clear-air spectral-polarimetric-variable distribution as input. The filter is applied to range-Doppler data. Fig. 4 shows all the steps of this filtering method. The first step consists of spectral polarimetric filtering using an optimized $s\rho_{\mathrm{co}}$ threshold value for each spectrogram. Then, the default Rijnmond notch filter is implemented to mitigate the ground clutter. Similar to the OBSpol filter, missing precipitation range-Doppler bins are reconstructed by mathematical morphology processing using the closing operator [8]. Finally, when the percentage of hydrometeor Doppler bins is very low, no data are attributed to the range bin. The following paragraphs dive into details of step 1, which is the innovative part, and this filtering technique is demonstrated for rain, clear-air, and saturated cases.

The first step removes most of the nonhydrometeors by giving a suitable threshold value. As concluded from Section III-E, $s\rho_{\mathrm{co}}$ is chosen to be the polarimetric spectrogram for thresholding. A square kernel (7×7) is used for

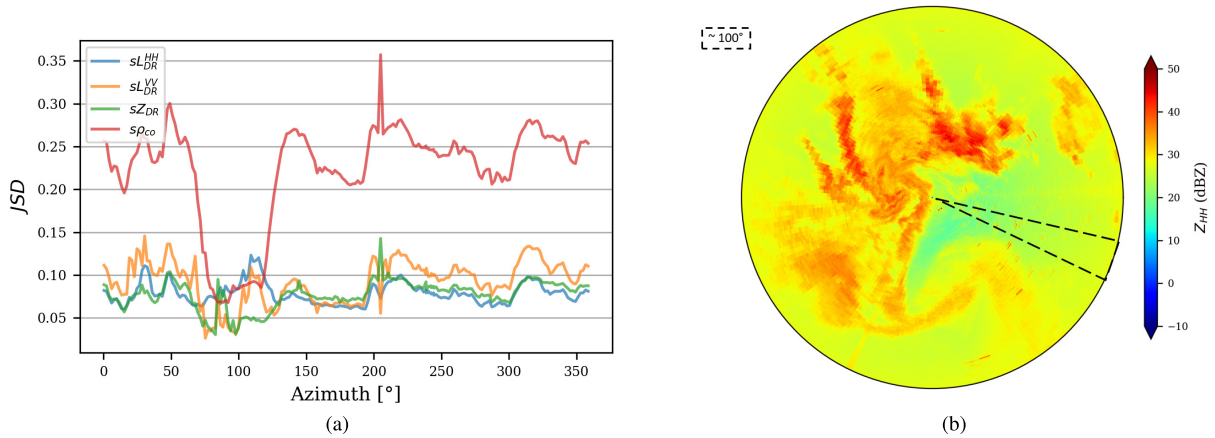

(a) (b)

Fig. 3. (a) JSD of different spectral polarimetric variables versus azimuth for rain case 2, which is represented by its nonfiltered reflectivity PPI in (b). Low values of JSD indicate similarity of the spectral polarimetric variable distribution with the corresponding reference mean clear-air distribution.

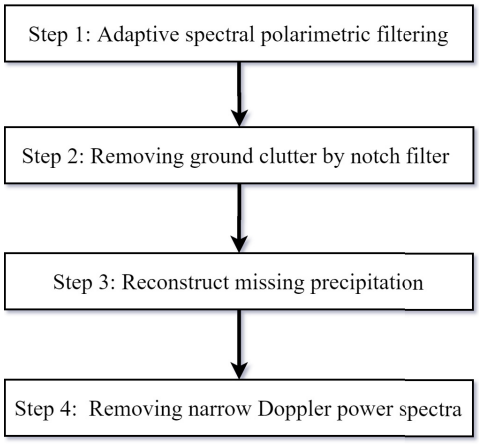

Fig. 4. JSD-based filtering algorithm.

the averaging in the estimation of $s\rho_{\text{co}}$ [see (5)]. After the threshold value is determined, a binary mask ($M^{s\rho_{\text{co}}}(r, v)$) is created

$$M^{s\rho_{\text{co}}}(r, v) = \begin{cases} 1, & \text{if } s\rho_{\text{co}} > T_{\text{opt}} \\ 0, & \text{otherwise} \end{cases} \tag{16}$$

where T_{opt} refers to the optimized threshold value of $s\rho_{\text{co}}$, **1** is the label for hydrometeors, and **0** is for nonhydrometeors. The threshold T_{opt} is determined for each spectrogram.

The critical part of this step is to determine the magnitude of $s\rho_{\text{co}}$ for thresholding. The optimized threshold magnitude T_{opt} is determined by the $s\rho_{\text{co}}$-distribution similarity and disparity between an input spectrogram and the averaged distribution of clear-air echo ($\overline{P_{\text{cla}}(s\rho_{\text{co}})}$). The nonhydrometeor part of a spectrogram is similar to the spectrogram of clear-air echoes. As a result, the $s\rho_{\text{co}}$-distribution of the nonhydrometeors is similar to the $s\rho_{\text{co}}$-distribution of clear air. In addition, there is a disparity of this distribution between hydrometeors and clear air. Those similarities and disparities are measured by JSD

$$\text{JSD}_U = \text{JSD}(P(s\rho_{\text{co}})_{M^{s\rho_{\text{co}}}=0} \| \overline{P_{\text{cla}}(s\rho_{\text{co}})}) \tag{17}$$

$$\text{JSD}_H = \text{JSD}(P(s\rho_{\text{co}})_{M^{s\rho_{\text{co}}}=1} \| \overline{P_{\text{cla}}(s\rho_{\text{co}})}) \tag{18}$$

$$\text{JSD}_D = \text{JSD}_H - \text{JSD}_U \tag{19}$$

where JSD_U denotes the JSD between the $s\rho_{\text{co}}$-distribution of the nonhydrometeor part of an input spectrogram ($P(s\rho_{\text{co}})_{M^{s\rho_{\text{co}}}=0}$) and the averaged $s\rho_{\text{co}}$-distribution of clear-air echo ($\overline{P_{\text{cla}}(s\rho_{\text{co}})}$). Also, JSD_H is the JSD between the $s\rho_{\text{co}}$ distribution of the hydrometeor part ($P(s\rho_{\text{co}})_{M^{s\rho_{\text{co}}}=1}$) and $\overline{P_{\text{cla}}(s\rho_{\text{co}})}$.

As the binary mask is a function of the threshold T and JSD is a function of the mask, the JSD corresponds to a function of T. We expect that the extracted nonhydrometeor $s\rho_{\text{co}}$-distribution is similar to the clear-air echo one and thus leads to a small JSD_U. Similarly, a discrepancy between the distributions of the extracted hydrometeor part and the clear-air echo one leads to a large JSD_H. Therefore, the optimized threshold value T_{opt} is selected when the difference (JSD_D) between the disparity (JSD_H) and similarity (JSD_U) reaches the maximum.

The algorithm finds a suitable threshold value, T_{opt} by maximizing the JSD difference (JSD_D). As input to the algorithm, a suitable range of $s\rho_{\text{co}}$ threshold values is given, based on [9, p. 517]. Thus, the default lower bound of this range, T_b, is set to be 0.8 and the maximum is 1. The increment, dT, is a variable affecting the tolerance of the result as well as the operation time, so it depends on the user's demand. In this work, a value of 0.01 is chosen for dT. Examples of this algorithm implementation on rain and clear-air spectrograms are shown next.

1) Rain Case: As can be seen in Fig. 5, both JSD_H and JSD_U increase monotonically with the $s\rho_{\text{co}}$ threshold value (T) for a rain spectrogram. A higher T contributes to adding more potential hydrometeor pixels to the nonhydrometeor group. Meanwhile, the hydrometeor pixels are tending to be purely hydrometeors. Therefore, larger T results in a decrease of similarity between the nonhydrometeor part of this input spectrogram and the clear-air echo spectrogram of reference (larger JSD_U). Also, the hydrometeor group $s\rho_{\text{co}}$-distribution has substantially more disparity with the reference clear-air echo distribution.

2) Clear Air (Including Saturation): Fig. 5 shows an example of JSD_H, JSD_U and JSD_D profiles for a clear-air spectrogram (including saturation). Clear air and saturation have similar spectral co-polar correlation coefficient

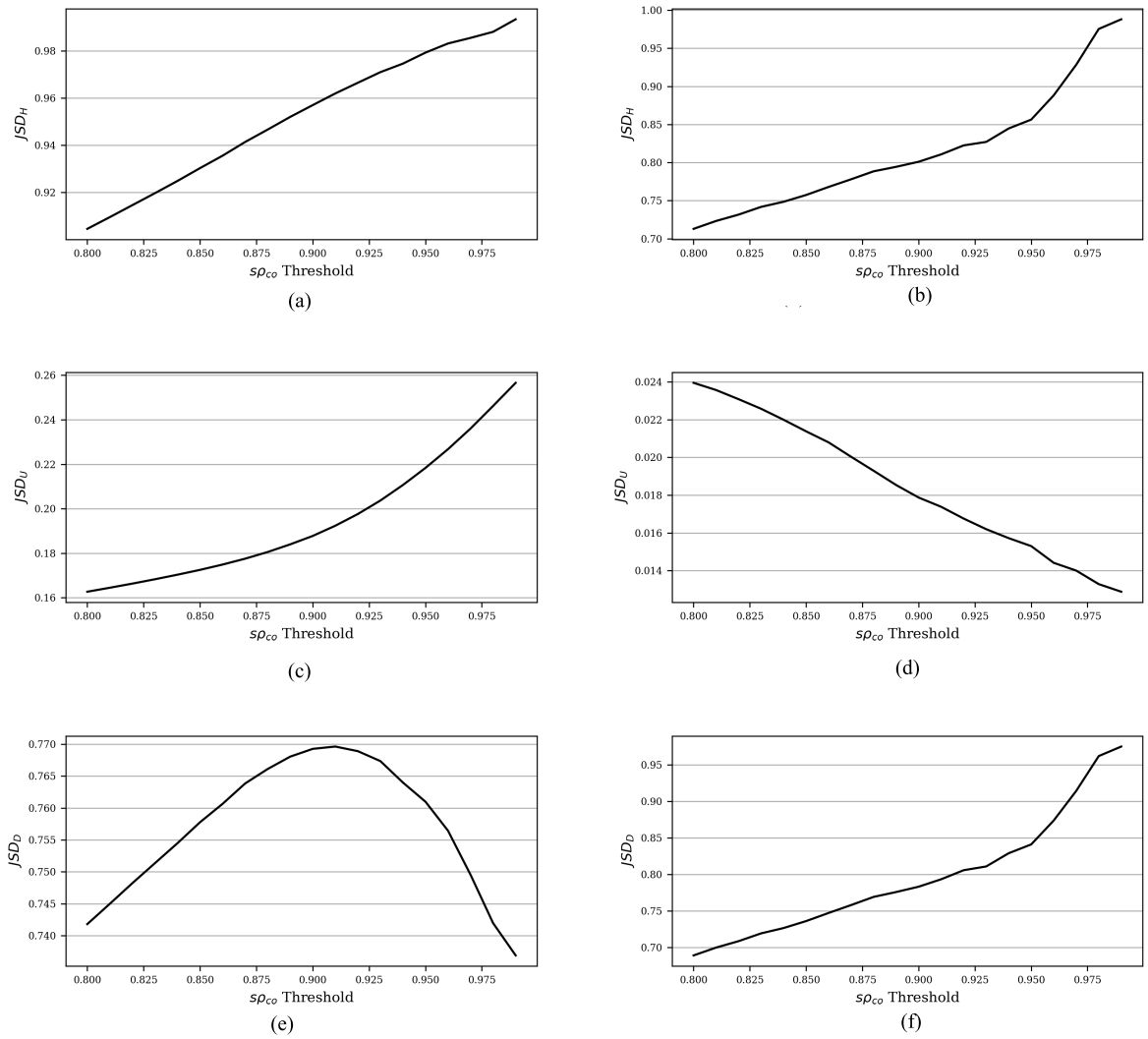

Fig. 5. JSD_H, JSD_U, and JSD_D profiles versus $s\rho_{\text{co}}$ threshold for T_{opt} determination. The left figures relate to a spectrogram with partial rain, and the right figures correspond to clear air (including saturation) only. For this rain spectrogram, the optimal value is $T_{\text{opt}} = 0.91$. For the clear-air spectrogram, the optimal value is $T_{\text{opt}} = 1.00$. (a) Rain JSD_H profile. (b) Clear-air JSD_H profile. (c) Rain JSD_U profile. (d) Clear-air JSD_U profile. (e) Rain JSD_D profile. (f) Clear-air JSD_D profile.

distributions (see Fig. 2) and lead to the same results in terms of JSD_H, JSD_U, and JSD_D. As the characteristics of an input spectrogram are initially unknown, an input spectrogram is treated as a spectrogram with hydrometeors by the algorithm. As T increases, the JSD_H values have the same tendency as a rain spectrogram. However, the similarity is high between the tested nonhydrometeor part and the reference clear-air spectrogram (very low values of JSD_U). For JSD_U, the minimum is reached when the whole spectrogram is labeled as nonhydrometeors ($T = 1$). At the same time, JSD_D has reached its maximum. Therefore, a clear-air (with/without saturation included) spectrogram is totally filtered by this algorithm.

IV. How to Evaluate a Filter Without Ground Truth?

Unsupervised evaluation metrics from image segmentation are used in this article for the first assessment of filtering without ground truth. With this methodology, the optimization of filtering parameters can be performed. As a start, assessment criteria should be defined. Without such assessment criteria, it is hard to determine whether a filter performs well or not when designing and testing different filters. The filtering of nonhydrometeors occurs in the range-Doppler domain. Therefore, criteria of good segmentation are defined in the spectral domain. However, residual nonhydrometeor range-Doppler bins may stay after this mitigation leading to badly estimated radar moments data at some ranges, which may be misinterpreted as rain. Consequently, it is necessary to define assessment criteria for good segmentation in the time domain as well.

To assess the filtering techniques, equivalently on the segmented spectrogram, subjective and objective evaluations are used. The difference between them consists of whether having human evaluation involved or not.

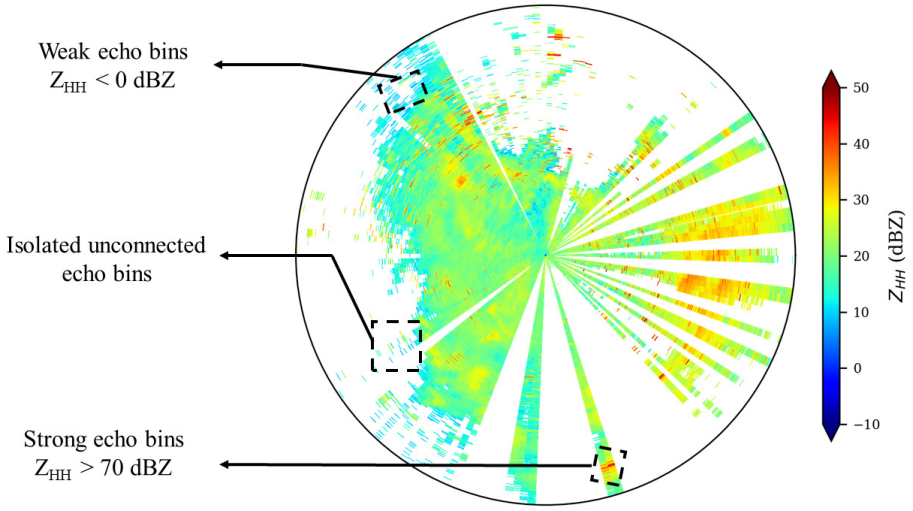

Fig. 6. Examples of three types of unwanted echoes (nonhydrometeors) in a badly filtered PPI of reflectivity.

A. Assessment Criteria in the Spectral Domain

For image segmentation, widely used assessment criteria exist [17]. These general image segmentation criteria are adapted for the application of nonhydrometeor filtering in the radar spectral domain. Using the assumption of range-Doppler continuity of precipitation and the specificity of polarimetric spectrograms, the image segmentation criteria are defined as follows.

1) Segmented hydrometeor and nonhydrometeor regions should be uniform and homogeneous concerning their spectral polarimetric features (e.g., intensity).
2) Boundaries between hydrometeors and nonhydrometeors should not be ragged and should be spatially accurate.
3) Hydrometeor region interiors should be without holes and with a spatial connection.

B. Assessment Criteria in the Time Domain

The above criteria are all for spectrogram images, which provide a radar variable versus range and Doppler velocity at a specific azimuth or time. However, the final representation of weather radar data, such as PPI, is in the time domain instead of the spectral domain. Here, the integrated variable is given versus range at a specific azimuth or time. The time-domain reflectivity (Z_{HH}) at each range bin results from the summation on spectral bins. Therefore, if a few range-Doppler bins exist at one range, this will result in one echo bin in the time domain. Even with a high performance of the filters in clear-air echo suppression in the spectral domain, some PPI rays may thus still contain unwanted signals in the time domain.

Assuming that rain bins are continuous, regardless of the spectral or time domain, isolated unconnected echo bins are accordingly considered as badly filtered. Furthermore, it can be assumed that Z_{HH} values lower than 0 dBZ and larger than 70 dBZ can be classified as nonhydrometeors [9]. The relatively low occurrence of such echoes in range bins is an indicator of good filtering. Examples of isolated unconnected echoes, both for weak and strong reflection, are shown in Fig. 6. Therefore, the following three criteria in the time domain are formulated.

1) All echo bins should be removed in the time domain when they relate to clear-air echoes.
2) The number of nonhydrometeor echoes should be zero or minimal.
3) The number of nonconnected echoes should be zero or minimal.

C. Subjective Evaluation

The application of subjective evaluation methods is limited. The segmented results are qualitatively assessed by human evaluation: for example, by only looking at a filtered spectrogram or PPI. Due to the necessary human intervention, this method is time-consuming when the dataset is large and thus excludes real-time assessment.

D. Objective Evaluation

Objective evaluation methods are those without human evaluation [18]. From previous studies [7], [8], typically, the used objective evaluation method is the supervised evaluation, which compares the segmented results with given ground-truth data. With radar-based precipitation spectrograms, there is no reference to ground-truth pixels. In addition, artificially generating such reference data is challenging [8] and subjective to errors. Such methods that use artificial reference data evaluate a segmented image by a set of characteristics as desired by humans [18]. Unsupervised methods are thus necessary to develop.

Unsupervised methods matching the criteria in Sections IV-A and IV-B are introduced in the following. Each objective evaluation method will be matched with each criterion. S and T refer to spectral and time domains, respectively, and the accompanying number relates to the criterion order. For example, S-1 means the number 1 criterion in the spectral domain.

TABLE III
OVERVIEW OF THE USED FILTER PARAMETERS

Filter Technique	Rijnmond Default Filter	OBSpol Filter	JSD based Filter
Thresholding condition for hydrometeor	$s\rho_{co} > 0.95$	$s\rho_{co} > 0.95$	$s\rho_{co} > T_{opt}$
Other empirical parameters	Noise clipping threshold: 3 dB Minimum Doppler bin ratio: 2% Notch filter width: 0.2 m s^{-1}	Structural element radius: 3 Hydrometeor objects number: 8 Non-stationary clutter Doppler width: 42 cm s^{-1}	Minimum Doppler bin ratio: 2% Notch filter width: 0.2 m s^{-1}
Prerequisite	Noise power measurement	None	Clear air echo database.

Two segmentation concepts will be used in this section: oversegmentation and undersegmentation. An oversegmented object has all its pixels correctly labeled, but it misses pixels, which are grouped in other objects. The undersegmented object has its pixels with correct and incorrect labels, which means that a part of its pixels should belong to other objects.

1) Uniformity Measurement (Criterion S-1):

1) *Method:* Criterion S-1 states that the segmented areas should be uniform with their own characteristics, such as the distribution of spectral polarimetric variables. More uniformity within an object is an indication of less contamination of unwanted echoes inside. The region Shannon's entropy H_v [19] is used to assess the uniformity within each region and is defined as

$$H_v(R, X) = \sum_{i=1}^{n} P(x_i) \log_2 \frac{1}{P(x_i)} \tag{20}$$

where $H_v(R, X)$ denotes the region entropy for the region R, X represents the assessed spectral polarimetric variable, and n is the number of probability function bins $P(x_i)$. The region entropy has been validated in studies and has shown good performance in classifying different objects in one image [18].

Here, we consider two types of regions, hydrometeors and nonhydrometeors, for which the expected region entropy H_r [19] is defined by summing each region entropy H_v multiplied by the weight proportional to the pixel numbers of that area S_j

$$H_r = \sum_{j=1}^{2} \left(\frac{S_j}{S_I} \right) H_v(R_j) \tag{21}$$

$$R_j \in \{R_C, R_H\} \tag{22}$$

$$S_j \in \{S_C, S_H\} \tag{23}$$

$$S_I = N_{\text{range}} \times N_{\text{Doppler}} \tag{24}$$

where R represents the label of the segmented regions and S is the area or pixel numbers of the region. The subscripts C and H of R_j and S_j denote nonhydrometeor (clutter) and hydrometeor, respectively. S_I is the total area of the whole range-Doppler spectrogram, which corresponds to the total pixel number. H_r represents the expected entropy across all regions, and its definition is based on Property 4 of Shannon's entropy.

A low entropy value corresponds to a limited number of spectral polarimetric variable values in the segmented region (Properties 2 and 3 of Shannon's entropy) [14]. A low entropy value is thus an indicator of uniformity for the spectral polarimetric variable that is considered. A larger entropy value refers to partial regions contaminated with pixels from unwanted echoes. As concluded from Section III-E, the distribution of $s\rho_{\text{co}}$ has the most sensitivity to the presence of rain in the spectrogram. Therefore, $s\rho_{\text{co}}$ is the spectral parameter to be chosen for the uniformity measurement.

As lower entropy values are considered better, the assessment only with H_v may prefer solely oversegmented objects. This is the rationale to use H_r, which, by definition, involves the entropy of all the considered classes. However, the uniformity measurement by the expected region entropy has also limitations. The area of nonhydrometeor objects may be much larger than the rain objects. In that case, the regional entropy from nonhydrometeors ($H_v(R_C)$) may be dominant in the expected region entropy result (H_r) and thus decrease the impact of the hydrometeor part ($H_v(R_H)$).

2) *Illustration:* Figs. 7–9 show the relations between a segmented co-polar correlation coefficient spectrogram, its distribution, its region entropy (H_v), and its expected region entropy (H_r) using two segmented results. Fig. 7(a) shows the raw polarimetric spectrogram chosen for segmentation. Two label masks [Fig. 7(b) and (c)] result from two different methods, OBSpol and JSD filters. Details of the filters are given in Table III. Figs. 8 and 9 show the uniformity measurement for these two masks. Although a fixed threshold for $s\rho_{\text{co}}$ is used (fixed for mask A and retrieved for mask B), lower/higher values of $s\rho_{\text{co}}$ are found in hydrometeor and nonhydrometeor histograms because of the mathematical morphological pixel reconstruction. Fig. 8 shows the $s\rho_{\text{co}}$ histograms and spectrograms of extracted hydrometeors and nonhydrometeors by mask A. On the one hand, the extracted hydrometeor area by mask A in Fig. 8(b) contains nonhydrometeor pixels that are ground clutter around 0 ms^{-1} or have low $s\rho_{\text{co}}$ values along the boundary of hydrometeor regions. This results in a $s\rho_{\text{co}}$ distribution with a long left tail in Fig. 8(d) and large $H_v(R_H, s\rho_{\text{co}})$. The segmented hydrometeor area by mask B [Fig. 9(b)] does not show nonhydrometeor pixels but lost some hydrometeor pixels. On the other hand, the segmented nonhydrometeor area by mask A [Fig. 8(a)] does not contain hydrometeor pixels, while the segmented one by mask B [Fig. 9(a)] shows pixels

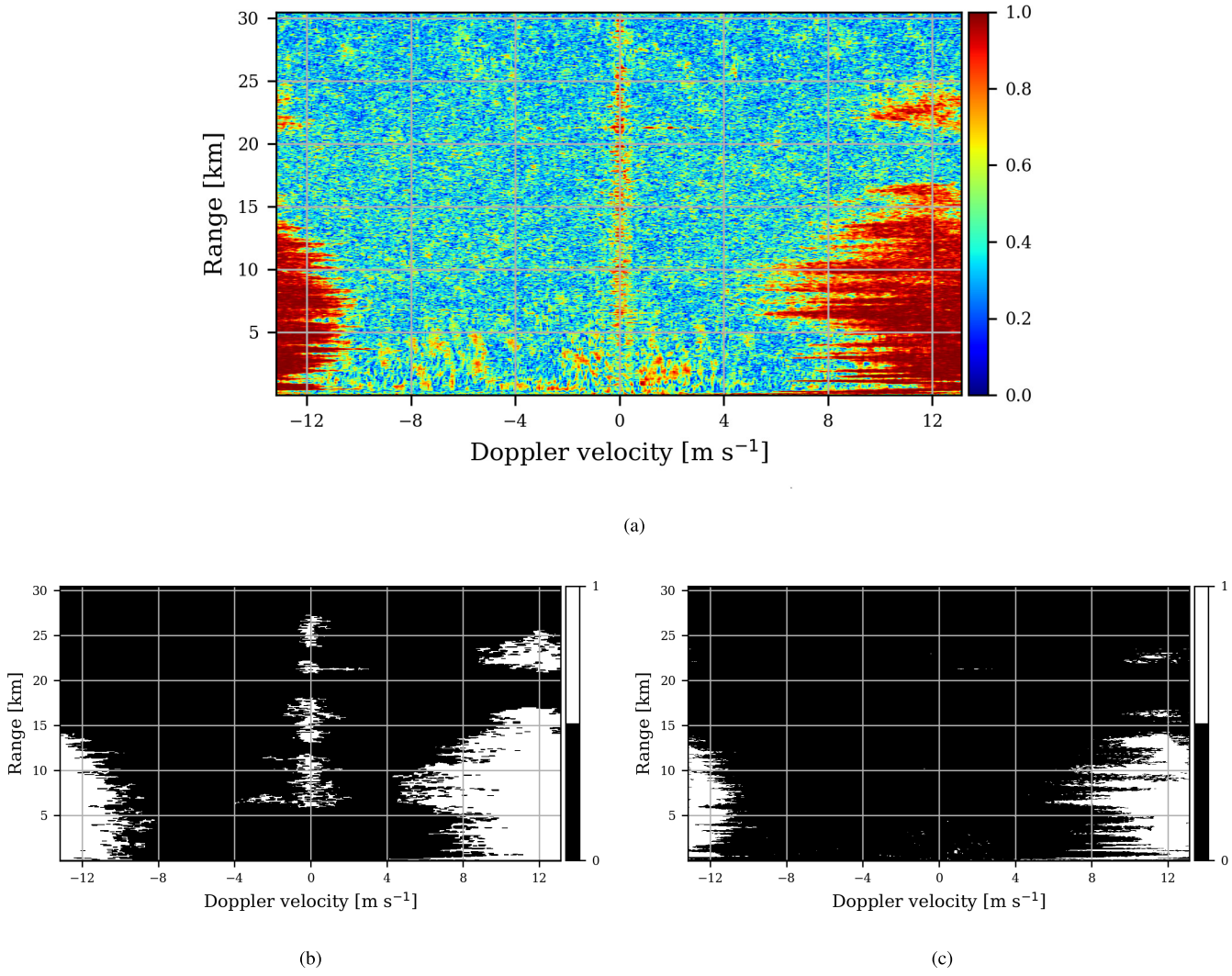

Fig. 7. Data correspond to Fig. 1(a) (rain case 1) at the azimuth 82.51°. (a) Raw spectral co-polar correlation coefficient. (b) Mask A (Filter OBSpol). (c) Mask B (Filter JSD).

with relatively high $s\rho_{\text{co}}$ values, which are potentially representing hydrometeors.

Summarizing, the segmented hydrometeor region by mask A suffers from undersegmentation (contains nonhydrometeor pixels) and the nonhydrometeor area is oversegmented. This is contrary to the result of mask B with an oversegmented hydrometeor and undersegmented nonhydrometeor regions. Their contamination levels are measured by H_r. For both masks, the regional entropy value is dominated by the large contribution of noise (part of nonhydrometeors) with a large area in the range-Doppler domain and a wide $s\rho_{\text{co}}$ distribution.

Because the ground truth is not known, we cannot say whether $H_r = 6.108$ (mask A) or 6.051 (mask B) is a good or bad value. It is a metric to relatively measure segmentation results, which shows the overall segmentation result and can thus overlook some local segmentation details. Therefore, using only this metric is not sufficient and more metrics should be developed.

2) Boundary Contrast (Criterion S-2):

1) *Method:* A local assessment based on Shannon's entropy is derived, to obtain a measure for boundary contrast. The first step is to find the spectrogram, which has a sharp boundary between the rain objects and nonhydrometeors. The boundary to distinguish rain from nonhydrometeors should exhibit a sharp change of smoothness: the rain object is smooth, while the nonhydrometeor area at the rain boundaries is typically noisy that translates into a large entropy. Based on subjective evaluation, sZ_{DR} is a suitable polarimetric spectrogram to consider.

How to define a boundary in a range-Doppler spectrogram? We want to calculate the entropy gradient through the boundary between the two objects. A high entropy gradient corresponds to a sudden change. For the rain object, we define the inner line as the pixel series with one-unit pixel width along the boundary inside the rain object. The outer line is the pixel series along the

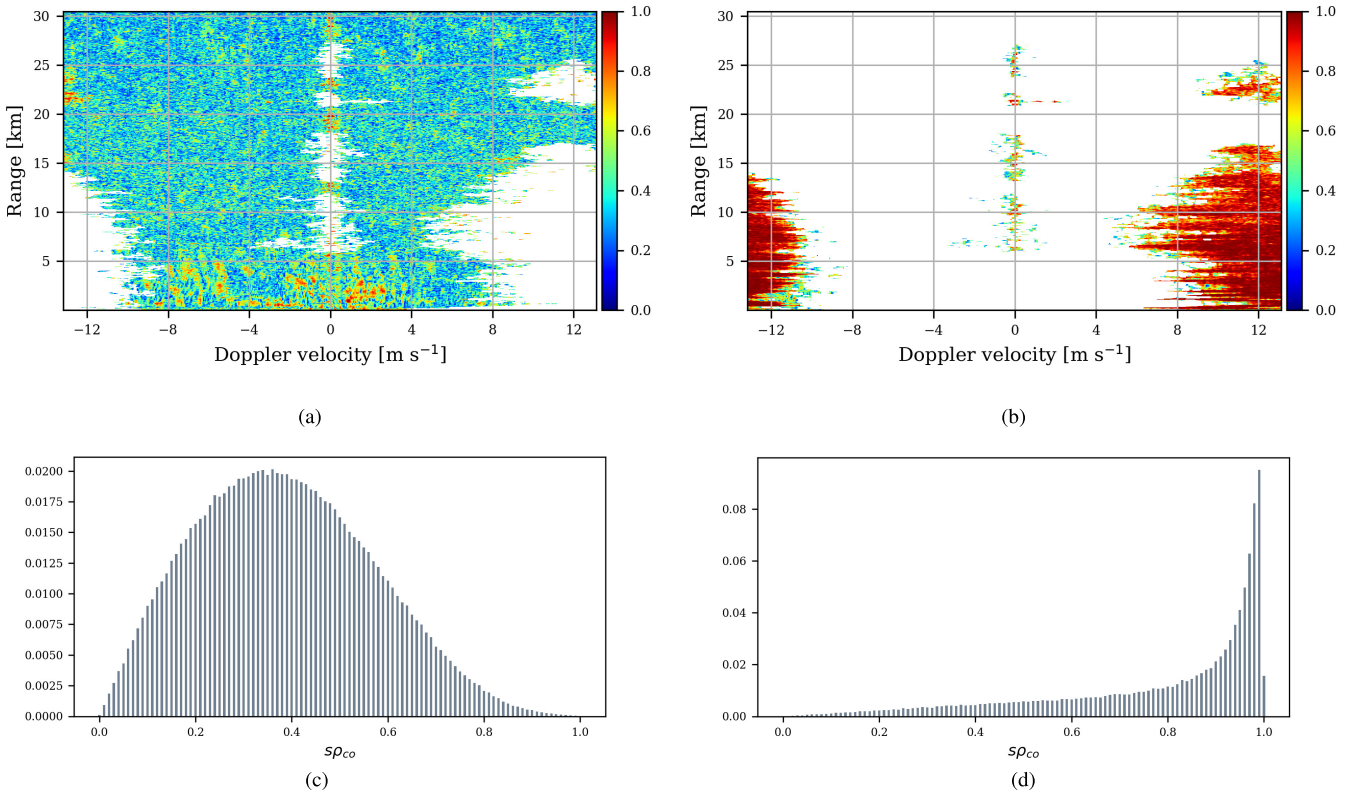

Fig. 8. Result of the segmentation of the co-polar correlation coefficient spectrogram by mask A. The regional entropy H_r equals 6.108. (a) $s\rho_{\text{co}}$: extracted nonhydrometeors by mask A. (b) $s\rho_{\text{co}}$: extracted hydrometeors by mask A. (c) $s\rho_{\text{co}}$ distribution of nonhydrometeors ($H_v(R_C, s\rho_{\text{co}}) = 6.192$). (d) $s\rho_{\text{co}}$ distribution of hydrometeors ($H_v(R_H, s\rho_{\text{co}}) = 5.727$).

boundary inside the nonhydrometeor object side. The expected entropy of each line is then defined as

$$H_v(L_j, sZ_{\text{DR}}) = \sum_{i=1}^{L_j} P(x_i) \log_2 \frac{1}{P(x_i)} \tag{25}$$

$$L_j \in \{L_{\text{in}}, L_{\text{out}}\} \tag{26}$$

where L is the pixel number of each line. The entropy gradient is the difference

$$H_d = H_v(L_{\text{out}}) - H_v(L_{\text{in}}). \tag{27}$$

There are two cases when the entropy gradient is lower, namely, oversegmented and undersegmented rain objects. In these cases, the boundary locates within the rain object or the nonhydrometeors, which leads to the inner and outer line to be in one object only. Consequently, the entropy gradient through the segmented boundary is small and points out a bad segmentation.

2) *Illustration:* Fig. 10 shows an example schematic of boundary contrast with pixel labeling: the top left is a 9×5 image that is part of the sZ_{DR} on the right. The labeling of the inner and outer line region is shown. We can see those pixels from the outer line region having large variations in the sZ_{DR} values, while the inner line pixels are more uniform (smoother).

3) Connectivity Measurement (Criterion S-3):

1) *Method:* Connectivity is defined by the ratio of the inner line pixel numbers, S_L, to the total pixel number of the hydrometeor objects, S_H. The inner line pixel is defined as the pixel with at least one neighbor pixel having a different label. If the connectivity is close to 1, this implies that the hydrometeor objects lose their spatial connectivity—more labeled hydrometeor pixels are isolated with neighboring nonhydrometeor pixels. The value of C ranges from 0 to 1

$$C = \frac{S_L}{S_H}. \tag{28}$$

2) *Illustration:* Fig. 11 shows two exemplary masks with different connectivities and their corresponding inner lines. All white or black pixels are connected in the first label mask [Fig. 11(a)] without any hole inside, so its connectivity value C is low. In the second mask [Fig. 11(c)], there are some holes within the object, so its connectivity value (C) is large.

4) Removal Percentage (Criterion T-1): A removal percentage (R_{rm}) is defined for each PPI ray. It is the key factor to nonhydrometeor filtering assessment in the case of clear-air measurement. Here, a qualitative ground truth is needed because no hydrometeor signal should be present in the PPI measurement. According to the first criterion in the time domain, a high removal percentage suggests a strong nonhydrometeor removing ability since all the signals in the clear-air are related to nonhydrometeors. The removal percentage is

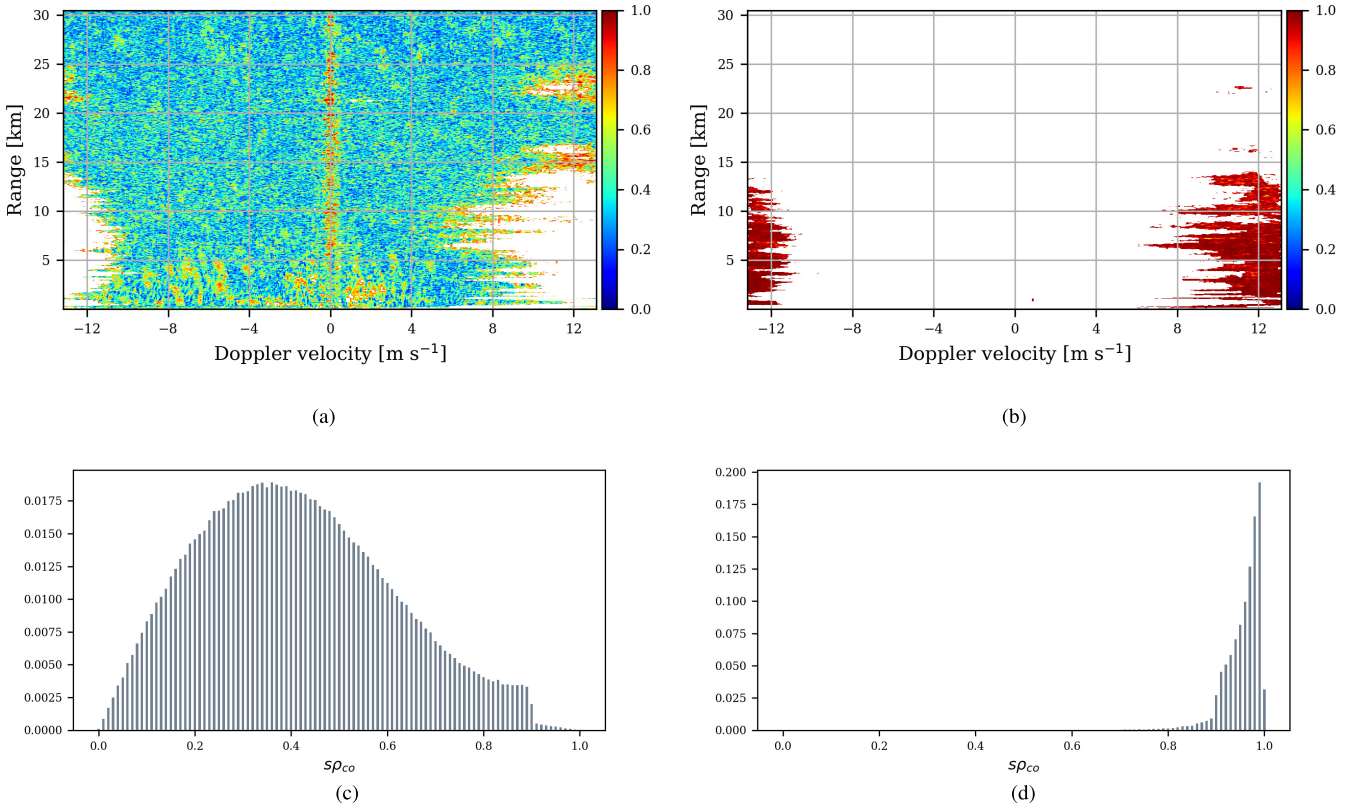

Fig. 9. Result of the segmentation of the co-polar correlation coefficient spectrogram by mask B. The regional entropy H_r equals 6.051. (a) $s\rho_{\text{co}}$: extracted nonhydrometeors by mask B. (b) $s\rho_{\text{co}}$: extracted hydrometeors by mask B. (c) $s\rho_{\text{co}}$ distribution of nonhydrometeors ($H_v(R_C, s\rho_{\text{co}}) = 6.298$). (d) $s\rho_{\text{co}}$ distribution of hydrometeors ($H_v(R_H, s\rho_{\text{co}}) = 3.539$).

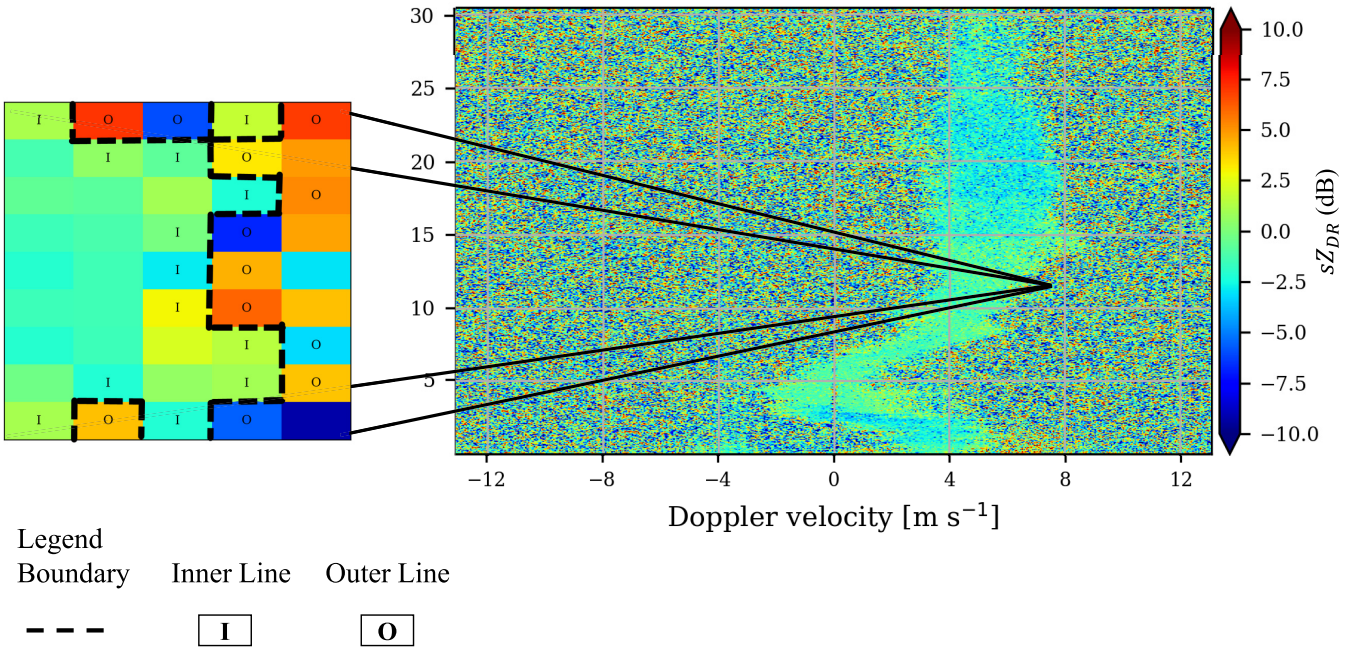

Fig. 10. Example schematic of boundary contrast. (Right) Spectral differential reflectivity in dB is shown with (Left) zoomed panel to illustrate the boundary contrast with pixel labeling.

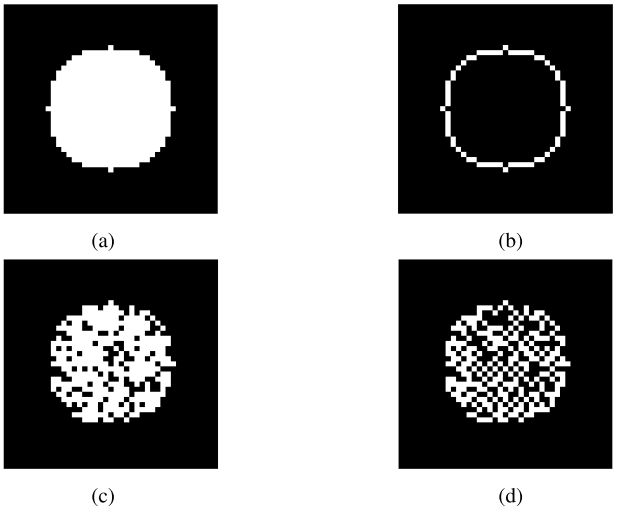

Fig. 11. Demonstration of connectivity measurement. (a) Mask 1 ($C = 0.146$). (b) Inner line of Mask 1. (c) Mask 2 ($C = 0.703$). (d) Inner line of Mask 2.

defined as

$$R_{\mathrm{rm}} = \frac{N_e}{N_{\mathrm{range}}} \tag{29}$$

where N_e denotes the number of echo bins in a radar ray and N_{range} is the total number of radar resolution volumes in the whole ray.

5) Weak and Strong Echo Ratio (Criterion T-2): The following defined factor relates to very low and high equivalent reflectivity factor values that are still present in the PPI ray after the filtering. These values are expected to correspond to nonhydrometeors. In particular, a PPI ray with reflectivity values above 70 dBZ may indicate saturation. The ratio related to the amount of weak and strong echoes in the whole radar ray is defined as

$$R_{\mathrm{ws}} = \frac{N_{\mathrm{ws}}}{N_{\mathrm{range}}} \tag{30}$$

where N_{ws} denotes the number of echo bins whose Z_{HH} is lower than 0 dBZ or larger than 70 dBZ.

6) Isolated Unconnected Echo Bin Ratio (Criterion T-3): According to the third criterion, a large number of isolated unconnected echo bins is considered as a bad filtering result. Here, we define the isolated unconnected echo bin ratio (R_{su}) as

$$R_{\mathrm{su}} = \frac{N_{\mathrm{su}}}{N_{\mathrm{range}}} \tag{31}$$

where N_{su} denotes the number of isolated unconnected range bins in the considered ray.

Summarizing, criteria T-1–T-3 relate to the evaluation of one ray in the PPI and criteria S-1–S-3 relate to the assessment of the corresponding polarimetric spectrograms, $s\rho_{\mathrm{co}}$ or sZ_{DR}.

V. Results

Subjective and objective methods are used to assess three filtering techniques, namely, the default Rijnmond filter (Section II-C) and JSD-based and OBSpol filter [8]. A summary of their parameters is given in Table III. Different scenarios given in Table II, clear-air echo and rain cases, are tested. For the evaluation result of each case and filter, one full PPI consisting of 196 rays is considered. The subjective method consists of plotting and visually assessing the filtered PPI. In the case of objective methods, the use of assessing variables depends on the tested scenarios. For example, considering clear air, the removal percentage, R_{rm}, is the appropriate assessing variable to test the filtering performance. Because of the lack of ground-truth data, objective evaluation variables in the spectral domain (H_r, H_d, C) can only give a relative assessment, which is, however, very useful for comparing different filters. The optimized results of these three spectral domain assessment variables can only be obtained with the ground truth. On the other hand, all time-domain evaluations (R_{rm}, R_{ws}, and R_{su}) can show an absolute assessment as we expect that the value of 0 is the best. One PPI has 196 rays, so every study case provides 196 test results by each filter for all assessment variables. The distribution of each assessment variable is visualized by a boxplot [20]. When analyzing the boxplot, the median (Q_2 or the 50th percentile), interquartile range (IQR), and potential outliers (q_{out}) are considered. The IQR is defined as

$$\mathrm{IQR} = Q_3 - Q_1 \tag{32}$$

where Q_3 and Q_1 denote the 75th percentile and 25th percentile, respectively. Outliers (q_{out}) are those values that fulfill the conditions

$$q_{\mathrm{out}} \in \{q | q > Q_3 + 1.5 \times \mathrm{IQR}\} \tag{33}$$

$$q_{\mathrm{out}} \in \{q | q < Q_1 - 1.5 \times \mathrm{IQR}\} \tag{34}$$

where q denotes any value of one assessment variable among the 196 results for clear air (one test case) and 196×6 for rain (six test cases). Both IQR and number of potential outliers characterize the performance of the different filtering techniques.

A. Subjective Evaluation

The subjective evaluation method is used according to the criteria for time-domain radar profiles in Section IV-B. Besides, some radar rays suffer from saturation, so the ability of removing those saturation radar rays should also be considered. Figs. 12 and 13 show the raw data and filtered reflectivity results for two rain cases. Overall, all filters succeed in removing radar rays with saturation. Filter JSD retains the most radar bins with precipitation. Coming back to case 1, the optimized threshold, T_{opt}, of the spectral co-polar correlation coefficient (JSD-based filter) is plotted versus azimuth in Fig. 14. These values of T_{opt} explain that the fixed threshold of 0.95 is too high for this event and why so many precipitation bins are discarded by the default Rijnmond and OBSpol filter.

B. Objective Evaluation

1) Clear-Air Case: For the clear-air case evaluation, just the removal percentage (R_{rm}) in the time domain is considered. Fig. 15 shows the boxplots quantifying the statistical

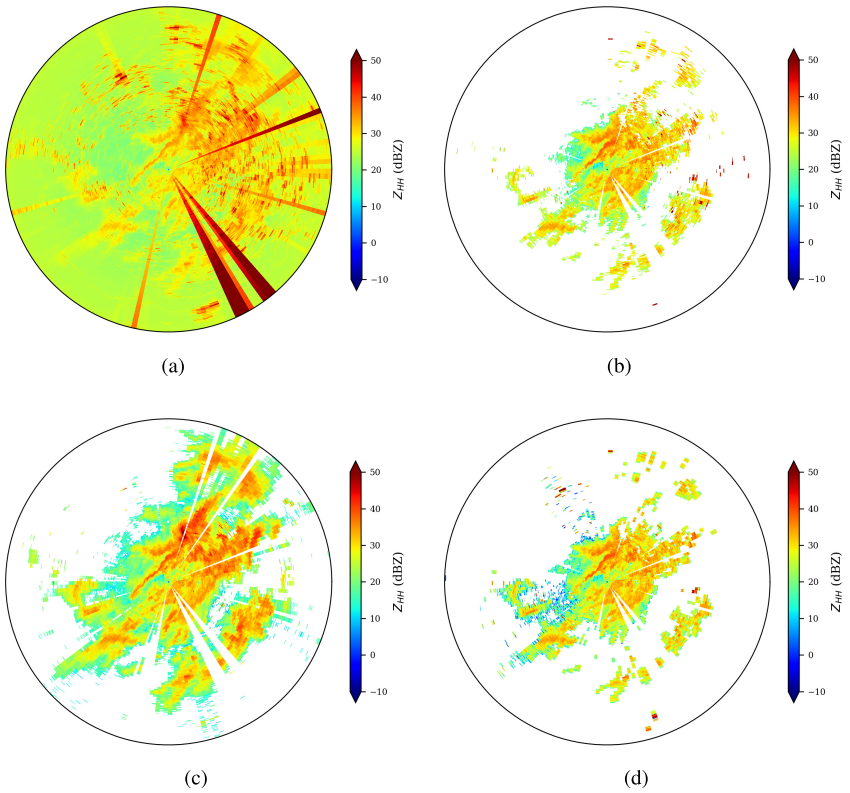

Fig. 12. Reflectivity PPIs (raw and filtered) for rain case 1. (a) Raw PPI. (b) PPI using the default Rijnmond filter. (c) PPI using the JSD-based filter. (d) PPI using the OBSpol filter.

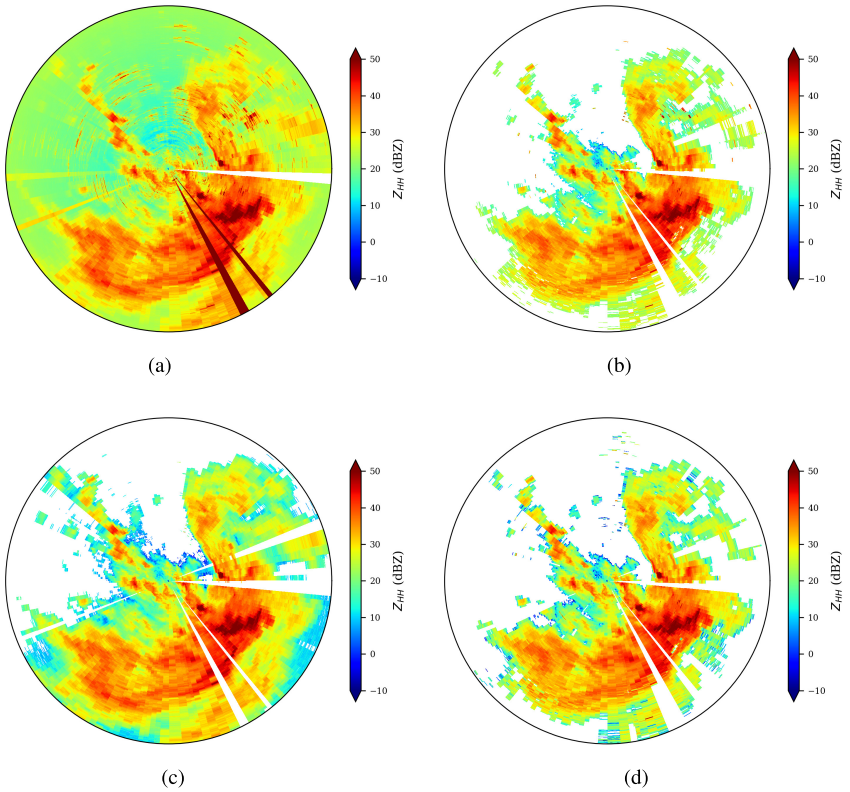

Fig. 13. Reflectivity PPIs (raw and filtered) for rain case 4. (a) Raw PPI. (b) PPI using the default Rijnmond filter. (c) PPI using the JSD-based filter. (d) PPI using the OBSpol filter.

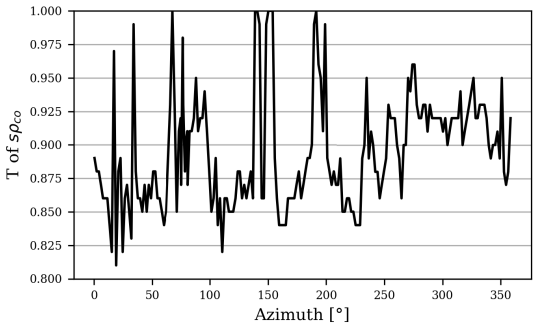

Fig. 14. Optimized threshold (T_{opt}) value as function of azimuth [for the PPI in case 1, Fig. 12(c)].

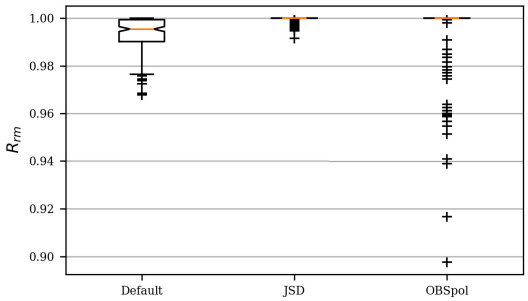

Fig. 15. Removal percentage results for the three filtering techniques. This parameter is only relevant for clear-air assessment.

performance of the three filters in removing nonhydrometeors. JSD and OBSpol filters can filter most of the clear-air echoes. Nonetheless, Filter JSD has the best performance because few outliers remain in the distribution. This result can be expected because JSD has as input a mean distribution of clear air. Consequently, if the clear-air distribution is quite stable in time and space, this is an efficient way to remove clear-air echoes.

2) Rain Cases Evaluation: Except for the removal percentage assessment, all evaluation methods in the spectral and time domain are considered and applied to all rain cases from Table II.

1) *Spectral Domain Evaluation Results:* Fig. 16 shows the regional entropy H_r distribution of the three filters. Filter JSD has the lowest median and a larger portion of radar rays distributed in lower H_r. The distributions of the other two filters are comparable. A lower H_r value suggests less contamination of unwanted echoes, either in the hydrometeor part or in the nonhydrometeor region. Therefore, filter JSD performs better in the classification with regard to the other two filters. However, the magnitude of H_r resulting from the three filters is comparable. This is due to the fact that H_r is dominated by $H_v(R_C)$ for each spectrogram. Coming back to Fig. 7, $H_v(R_H)$ of mask A is much larger than that of mask B, as the segmented hydrometeor region by mask A is more contaminated than that of mask B. Nonetheless, their nonhydrometeor regions show a similar level of uniformity, leading to comparable H_r values due to the large weight of the nonhydrometeor part.

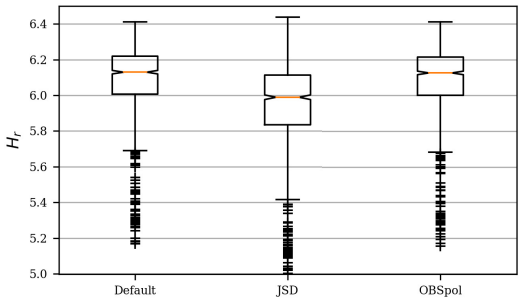

Fig. 16. Regional entropy results.

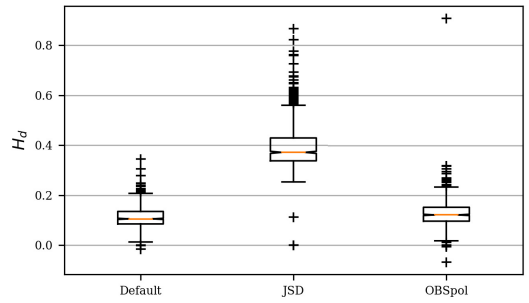

Fig. 17. Boundary contrast results.

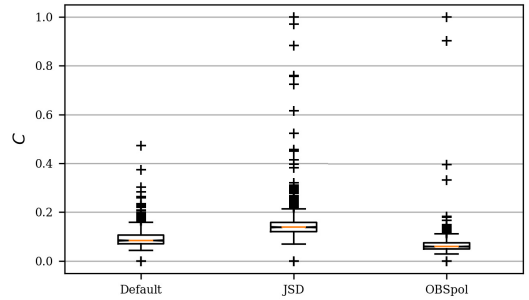

Fig. 18. Connectivity results.

For the boundary contrast (H_d) and spectral connectivity (C) assessment in Figs. 17 and 18, Filter JSD takes the highest values, while the performance between the other two filters is still similar. Higher H_d values show that the boundary position between hydrometeors and nonhydrometeors is more spatially correct, and higher C values refer to poorer connectivity. Because the JSD filter retains more precipitation, also weak precipitation in the form of isolated range-Doppler bins passes the filter, which increases the connectivity.

Summarizing, comparing the three filters, the JSD-based filter has better performances in terms of regional uniformity for hydrometeors and nonhydrometeors and boundary position between hydrometeor and nonhydrometeor areas. Nonetheless, it keeps a bit more isolated hydrometeor regions in the spectrograms.

2) *Time-Domain Evaluation Results:* For the time-domain evaluation, the three filters perform well and rather similar in terms of removal of weak and strong echoes

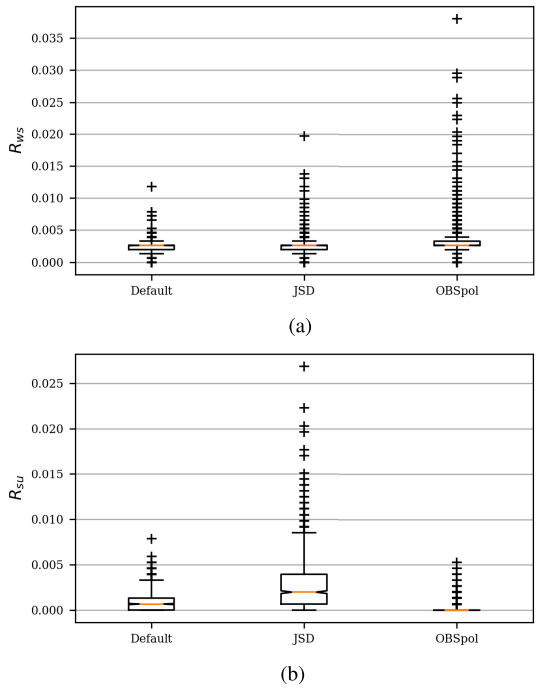

Fig. 19. Time-domain evaluation results of the three filtering techniques. (a) Ratio of weak and strong echoes results. (b) Ratio of isolated unconnected bins results.

[R_{ws} in Fig. 19(a)]. The values of this assessment parameter are very low with a median value of about 0.0025, and thus, 0.25% of weak and strong echoes are left in the PPI. Filter OBSpol has more radar rays with high R_{ws} than the other two filters. Although the R_{su} values are very low, the performance difference becomes larger for the time-domain connectivity, R_{su}, in Fig. 19(b), where the JSD filter has the most isolated unconnected echo bins and OBSpol filter the least. R_{su} is highly correlated with the spectral domain connectivity measurement, C. Summarizing, the JSD-based filter performs a bit less in terms of weak and strong echoes as well as isolated range bins removal. This is the price to pay for keeping as much precipitation as possible while mitigating a large quantity of nonhydrometeors.

VI. Discussion

In this section, we summarize and discuss the three filter performances from the subjective and objective evaluation results given in Section V.

As shown in Figs. 12 and 13, all three filters succeed in removing radar bins with saturation issues, which suggests that $s\rho_{\text{co}} = 0.95$ is sufficient for tackling this problem. However, $s\rho_{\text{co}} = 0.95$ is not enough to remove all unwanted echoes in the clear-air case and may discard precipitation areas in the rain cases. The default Rijnmond filter retains more clear-air radar bins than the other two filters (Fig. 15) since both the JSD and OBSpol filters benefit from morphological image processing. The JSD filter performs even better than the OBSpol filter because the JSD filter makes use of the $s\rho_{\text{co}}$ distribution of clear air. In terms of clear-air echoes, it means that this distribution is rather stable.

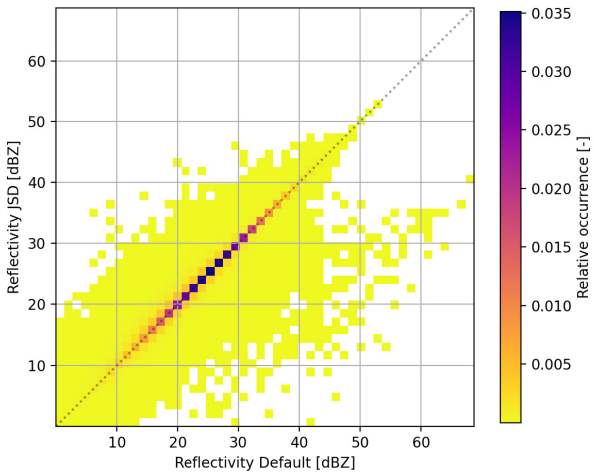

Fig. 20. Scatter density plot of reflectivity. The intensity shows the relative occurrence for all the study cases. The x-axis represents reflectivity values for the default Rijnmond filtering, and the y-axis represents reflectivity values for the JSD filtering.

In the rain case results, the default Rijnmond filter and OBSpol filter perform similarly considering either the subjective or objective results. Better results of regional entropy, H_r, and boundary contrast, H_d, verify that the JSD filter provides an improved separation between hydrometeors and nonhydrometeors in the spectrograms. One possible drawback of the Filter JSD is to keep narrow Doppler spectra or wider gaps in the spectra, which increases the connectivity parameter, both in the spectral and time domain. Overall, the JSD filter keeps more precipitation bins than the other two filters. Looking at the PPI of Fig. 12, we clearly see that a significant part of the precipitation with high reflectivity values is recovered while applying the JSD filter. Fig. 14, which relates to Fig. 12(c), shows that most of the threshold values are lower than 0.95. The same recovery happens in Fig. 13 for precipitation behind the largest reflectivity rain, where the values of spectral co-polar correlation coefficient are decreased because of the lowering in SNR due to attenuation. Such a precipitation recovery is mainly due to the fact that the JSD filter uses optimized threshold values. Again, providing a fixed threshold value for a radar measurement is somewhat tricky because the threshold depends on so many things, such as radar system, processing, measured hydrometeors (rain, melting layer, and so on), SNR, and environment around the radar. In this article, it is shown that adaptive thresholding within reasonable boundaries overcomes this issue.

One possible limitation of the JSD filter is the prerequisite of clear-air echo database. From February to October 2020, the same reference PPI of clear-air echo was used for the first tests of the JSD filter. However, the time variability of the clear-air echo database should be examined. The measurement of the raw data PPI is simple and the acquisition of the spectral co-polar correlation coefficient histrogram is straightforward. In the case of a radar network, a clear-air echo database is necessary for each radar.

One concern with the upgrade to the JSD filtering technique is whether the radar moments, such as reflectivity, are affected.

Fig. 20 shows a scatter density plot of the reflectivity with the JSD filter versus the original reflectivity using the default Rijnmond filter. This plot shows that an upgrade to the JSD filter does not change the estimation of the radar reflectivity for the majority of the radar range bins. Only for a minor portion of the range bins (e.g. clutter bins), the estimation is changed. The high reflectivity pixels, suspected to be clutter pixels, range from 55 to nearly 70 dBZ and appear in the scatter density plot for the default Rijnmond filter. These high reflectivity pixels are significantly reduced using the JSD filter and, as a result of this filter, range from 20 to 40 dBZ. This scatter plot also shows that the chosen case studies have a wide variety in reflectivity values (0–50 dBZ), which proves that sufficient statistics have been collected for a first good evaluation of the JSD filter.

VII. Conclusion

This article proposes a new filtering technique to extract hydrometeors and new unsupervised evaluation methods to assess filtering technique performance. This new filtering technique makes use of spectral polarimetry. Because of its bimodal distribution in the range-Doppler spectrogram when hydrometeors are present, the spectral co-polar correlation coefficient, $s\rho_{\text{co}}$, is selected. First, global thresholding is performed by an optimized threshold value, which is determined from the comparison of $s\rho_{\text{co}}$ distribution of the input spectrogram with the averaged $s\rho_{\text{co}}$ distribution of clear-air echoes. The methodology uses the JSD, which compares the similarity and discrepancy between distributions. After thresholding, a binary mask classifying hydrometeors and nonhydrometeors is obtained and the following steps are conducted sequentially to improve this classification result: notch filtering at 0 ms^{-1}, mathematical morphological processing, and narrow Doppler spectra filtering.

The new unsupervised evaluation metrics are derived from insights from emerging image segmentation techniques. For example, spectral polarimetric pixel labeling is similar to image segmentation. Before designing evaluation metrics, six criteria are defined in two domains, spectral and time, which are involved in the weather radar data processing pipeline. Accordingly, six unsupervised evaluation metrics are developed.

The performance of the new filter was compared with two other filters. Results show filtering improvement with the new filter both for clear-air and rain cases. Consequently, these new ideas are being implemented in the real-time software SkyTorque, which is used for three X-band radars (Rijnmond, MESEWI, and IDRA).

The discussed metrics allow a first assessment of filtering techniques in the range-Doppler and time domain. Consequently, several techniques with different parameterizations can be investigated in the context of urban clutter. This results in the preselection of one or a group of filtering techniques. The proposed methodology does not replace radar variable bias analysis using clutter data and rain data free of clutter and/or a QPE validation technique such as the validation of weather radar data with rain gauges, which has still to be carried out afterward.

This research was performed in the context of X-band radars having high spatial resolution and a limited maximum range. It would be worthwhile to investigate the proposed methodology for S- or C-band weather radars with large resolution volumes and maximum ranges. In addition, a high Doppler resolution was used, where 512 time samples were collected for Doppler processing. This number can be decreased by a factor of 2 while achieving the same performance. It is clear that spectral processing takes advantages of high Doppler resolution to disentangle in the time-domain signal, hydrometeors, clutter, and noise. Therefore, there is a tradeoff between fast-scanning weather radars with a low Doppler resolution and weather radars with a high Doppler resolution (scanning slower).

Acknowledgment

The authors thank the Co-Founder of SkyEcho, Yann Dufournet, for his support.

References

[1] *Economic Losses and Fatalities From Weather- and Climate-Related Events in Europe*, European Environment Agency, Copenhagen, Denmark, 2022.

[2] Y. Dufournet, A. O. Nijhuis, I. Stepanov, C. Unal, and H. Russchenberg, "Enhanced urban rain surveillance systems for smart city solutions—EU-rainS4," in *Proc. ATTRACT Final Conf.*, 2019, pp. 1–2.

[3] S. M. Torres and D. A. Warde, "Ground clutter mitigation for weather radars using the autocorrelation spectral density," *J. Atmos. Ocean. Technol.*, vol. 31, no. 10, pp. 2049–2066, 2014.

[4] D. Moisseev, C. Unal, H. Russchenberg, and L. Ligthart, "Doppler polarimetric ground clutter identification and suppression for atmospheric radars based on co-polar correlation," in *Proc. 13th Int. Conf. Microw., Radar Wireless Commun. (MIKON) Conf.*, May 2000, pp. 94–97.

[5] C. Unal, "Spectral polarimetric radar clutter suppression to enhance atmospheric echoes," *J. Atmos. Ocean. Technol.*, vol. 26, no. 9, pp. 1781–1797, 2009.

[6] D. N. Moisseev and V. Chandrasekar, "Polarimetric spectral filter for adaptive clutter and noise suppression," *J. Atmos. Ocean. Technol.*, vol. 26, no. 2, pp. 215–228, 2009.

[7] J. Yin, C. M. H. Unal, and H. W. J. Russchenberg, "Narrow-band clutter mitigation in spectral polarimetric weather radar," *IEEE Trans. Geosci. Remote Sens.*, vol. 55, no. 8, pp. 4655–4667, Aug. 2017.

[8] J. Yin, C. Unal, and H. Russchenberg, "Object-orientated filter design in spectral domain for polarimetric weather radar," *IEEE Trans. Geosci. Remote Sens.*, vol. 57, no. 5, pp. 2725–2740, May 2019.

[9] V. N. Bringi and V. Chandrasekar, *Polarimetric Doppler Weather Radar*. Cambridge, U.K.: Cambridge Univ. Press, 2011.

[10] F. Nai, S. Torres, and R. Palmer, "On the mitigation of wind turbine clutter for weather radars using range-Doppler spectral processing," *IET Radar, Sonar Navigat.*, vol. 7, no. 2, pp. 178–190, 2013.

[11] Y. Li, G. Zhang, and R. J. Doviak, "A new approach to detect the ground clutter mixed with weather echoes," in *Proc. IEEE Radar Conf.*, May 2011, pp. 622–626.

[12] C. M. H. Unal and D. N. Moisseev, "Combined Doppler and polarimetric radar measurements: Correction for spectrum aliasing and nonsimultaneous polarimetric measurements," *J. Atmos. Ocean. Technol.*, vol. 21, no. 3, pp. 443–456, Mar. 2004.

[13] C. E. Shannon, "Communication theory of secrecy systems," *Bell Labs Tech. J.*, vol. 28, no. 4, pp. 656–715, Oct. 1949.

[14] J. Chen, B. Guan, H. Wang, X. Zhang, Y. Tang, and W. Hu, "Image thresholding segmentation based on two dimensional histogram using gray level and local entropy information," *IEEE Access*, vol. 6, pp. 5269–5275, 2017.

[15] D. M. Endres and J. E. Schindelin, "A new metric for probability distributions," *IEEE Trans. Inf. Theory*, vol. 49, no. 7, pp. 1858–1860, Jul. 2003.

[16] J. Lin, "Divergence measures based on the Shannon entropy," *IEEE Trans. Inf. Theory*, vol. 37, no. 1, pp. 145–151, Jan. 1991.
[17] R. H. Haralick, "Survey-image segmentation techniques, computer vision," *Graph. Image Process.*, vol. 12, pp. 60–73, 1980. [Online]. Available: https://ci.nii.ac.jp/naid/10003789064/en/
[18] H. Zhang, J. E. Fritts, and S. A. Goldman, "Image segmentation evaluation: A survey of unsupervised methods," *Comput. Vis. Image Understand.*, vol. 110, no. 2, pp. 260–280, 2008.
[19] H. Zhang, J. E. Fritts, and S. A. Goldman, "An entropy-based objective evaluation method for image segmentation," *Proc. SPIE*, vol. 5307, pp. 38–49, Dec. 2003.
[20] J. W. Tukey, *Exploratory Data Analysis. Preliminary Edition*. Reading, MA, USA: Addison-Wesley, 1970.

Cheng Chen received the B.Sc. degree in environmental engineering from Chung Yuan Christian University, Taoyuan, Taiwan, in 2014, and the M.Sc. degree in environmental engineering from the Delft University of Technology, Delft, The Netherlands, in 2021.

Christine M. H. Unal joined the Delft University of Technology, Delft, The Netherlands, in 1988, where she is currently a Research Scientist and a Lecturer. She was first at the International Research Centre for Telecommunications and Radar, Delft, where she focused on radar polarimetric calibration and radar spectral polarimetry. Since 2003, she applied the latter expertise to enhance the processing of atmospheric echoes. In 2012, she joined the Department of Geoscience and Remote Sensing and the Delft Climate Institute. Her research has orientated toward weather/atmospheric radar signal processing and searching for new retrieval techniques to estimate microphysical and dynamical properties of precipitation using ground-based radars. Since 2020, she has participated in the implementation of the national infrastructure, Ruisdael Observatory, in terms of cloud radars and microwave radiometers. Her research interest is cloud radar microphysical retrievals.

Albert C. P. Oude Nijhuis received the M.Sc. degree in meteorology and physical oceanography from the University of Utrecht, Utrecht, The Netherlands, in 2012, and the Ph.D. degree from the Delft University of Technology, Delft, The Netherlands, in 2019, with a focus on radar remote sensing of wind vector and turbulence intensity fields from raindrop backscattering.

He worked as a Satellite Remote Sensing Researcher at the Royal Dutch Meteorological Institute (KNMI), De Bilt, The Netherlands. After his Ph.D. degree, he started working as a Weather Data Scientist and Project Manager at SkyEcho, Losser, The Netherlands.